AGU PUBLICATIONS

JGR

Journal of Geophysical Research: Oceans

RESEARCH ARTICLE

10.1002/2014JC010357

Key Points:

- The resolution of microwave SST images is increased using a statistical model
- The model is based upon statistics learned from intermittent infrared images
- The enhanced SST images are used to estimate subsurface velocities

Correspondence to:
S. R. Keating,
s.keating@unsw.edu.au

Citation:
Keating, S. R., and K. S. Smith (2015), Upper ocean flow statistics estimated from superresolved sea-surface temperature images, *J. Geophys. Res. Oceans*, *120*, 1197–1214, doi:10.1002/2014JC010357.

Received 31 JUL 2014
Accepted 26 JAN 2015
Accepted article online 29 JAN 2015
Published online 23 FEB 2015

Upper ocean flow statistics estimated from superresolved sea-surface temperature images

Shane R. Keating[1] and K. Shafer Smith[2]

[1]School of Mathematics and Statistics, University of New South Wales, Sydney, New South Wales, Australia, [2]Center for Atmosphere-Ocean Science, Courant Institute of Mathematical Sciences, New York University, New York, New York, USA

Abstract Ocean turbulence on scales of 10–50 km plays a key role in biogeochemical processes, frontal dynamics, and tracer transport in the upper ocean, but our understanding of these scales is limited because they are too small to be resolved using extant satellite altimetry products. By contrast, microwave imagery of the sea-surface temperature field does resolve these scales and can be used to estimate the upper ocean flow field due to the strong correlation between the surface density field and the interior potential vorticity. However, because the surface density (or temperature) is a smoothed version of the geostrophic stream function, the resulting velocity field estimates are limited to scales of 100–300 km in the first few hundred meters of the water column. A method is proposed for generating superresolved sea-surface temperature images using direct low-resolution (microwave) temperature observations in combination with an empirical parameterization for the unresolved scales modeled on statistical information from high-resolution (infrared) imagery. Because the method relies only on the statistics of the small-scale field, it is insensitive to data outages due to cloud cover that affect infrared observations. The method enhances the effective resolution of the temperature images by exploiting the effect of spatial aliasing and generates an optimal estimate of the small-scale temperature field using standard Bayesian inference. The technique is tested in quasigeostrophic simulations driven by realistic climatological shear and stratification profiles for three contrasting regions at high, middle, and low latitudes. The resulting superresolved sea-surface temperature images are then used to estimate the three-dimensional velocity field in the upper ocean on scales of 10–50 km.

1. Introduction

In recent years, upper ocean flows on scales of tens of kilometers have become accessible to field observations and regional modeling studies. The emerging picture is surprisingly rich in fine-scale flow features characterized by strong surface intensification, frontogenesis, and enhanced vertical transport of nutrients, potential vorticity, and buoyancy. These scales strongly modulate biogeochemical processes, pollutant dispersal, and turbulent transport in the upper ocean [*Thomas et al*., 2008] and play a critical role in mediating the transfer of energy from balanced mesoscale eddies to smaller scales, where it is dissipated by three-dimensional processes [*Ferrari and Wunsch*, 2009]. However, direct global observation of the upper ocean on these scales is challenging: in situ measurements typically lack sufficient geographical coverage, while sea-surface velocities estimated from satellite altimetry do not currently have the spatial and temporal resolution required to resolve the features of interest.

High-resolution satellite observations of sea-surface temperature also preserve some information about the embedding turbulent flow. Satellite temperature measurements are of two broad types: infrared instruments such as the Advanced Very High-Resolution Radiometer provide daily observations on scales of kilometers but cannot penetrate cloud, and microwave instruments such as the TRMM Microwave Imager measure sea-surface temperature daily, regardless of cloud cover, with a coarser spatial resolution of 20–50 km. In either case, feature-tracking algorithms such as the gradient thresholding [*Holylr and Peckinpaugh*, 1989] or Maximum Cross-Correlation methods [*Emery et al*., 1986; *Bowen et al*., 2002] have been used to infer advective displacements between sequential satellite images. These techniques are essentially *kinematic* in nature—sea-surface temperature is treated as a passive tracer—and so their accuracy is limited by non-advective surface dynamics. Moreover, feature-tracking cannot be used to infer subsurface velocities.

Lapeyre and Klein [2006] introduced an alternate method for reconstructing upper ocean velocities based upon the surface quasigeostrophic (SQG) model, in which the interior geostrophic stream function is slaved to the surface temperature anomaly [*Blumen*, 1978; *Held et al*., 1995]. The technique estimates the interior potential vorticity anomaly from surface temperature measurements using an empirically derived vertical profile function calculated from the large-scale potential vorticity and surface temperature gradients. Once the interior potential vorticity is estimated, the subsurface horizontal stream function can be derived using the potential vorticity inversion principle [*Hoskins et al*., 1985]. The resulting stream function can then be used to calculate the horizontal velocity field and, via the omega equation, the vertical velocity [e.g., *Hoskins et al*., 1978]. Thus, the SQG method can be used to derive the three-dimensional velocity field in the upper ocean from individual microwave observations.

The SQG method estimates the contribution of surface dynamics to the full solution. However, the formalism can be modified to include the effect of interior dynamics through the use of an empirically derived effective buoyancy frequency [*Isern-Fontanet et al*., 2006, 2008], additional barotropic or baroclinic modes [*Lapeyre*, 2009; *Wang et al*., 2013], or a new basis set incorporating both surface and interior effects [*Smith and Vanneste*, 2013]. The SQG method effectively estimates the velocity field in the upper ocean (typically the first few hundred meters) when tested against in situ measurements [*LaCasce and Mahadevan*, 2006; *Isern-Fontanet et al*., 2006] and numerical simulations [*Lapeyre and Klein*, 2006; *Isern-Fontanet et al*., 2008; *Klein et al*., 2009; *Wang et al*., 2013]

In this paper, we will address a deficiency that is common to all SQG-based methods for reconstructing the subsurface flow: the need for very high-resolution sea-surface temperature observations. This arises because the SQG stream function is a smoothed version of the temperature field—high wavenumbers are suppressed relative to low wavenumbers. In consequence, microwave observations are capable of generating stream function estimates with a resolution of 100–300 km [*Isern-Fontanet et al*., 2006], comparable with that of satellite altimetry but insufficient to resolve the features of interest here. By contrast, infrared observations have spatial resolutions on the scale of kilometers, but these observations are frequently obscured by clouds and so are of limited utility.

Here, we propose a method for reconstructing high-resolution sea-surface temperature imagery using direct low-resolution (microwave) observations in combination with statistical information from high-resolution (infrared) observations. The method, *stochastic superresolution*, effectively enhances the resolution of temperature images by exploiting the fact that unresolved, small-scale temperature features are aliased into the resolved waveband of the image [*Majda and Grote*, 2007; *Harlim and Majda*, 2008; *Keating et al*., 2012; *Branicki and Majda*, 2013]. The method takes advantage of this aliasing effect by comparing the observed temperature with an empirical model based on the fine-scale statistics. The technique then uses standard Bayesian methods to generate an optimal estimate of the true temperature field by combining the observation and the prediction, weighted according to their relative uncertainties. Crucially, the resulting estimate has a resolution specified by the underlying empirical model, not the observations; in this way, it is possible to build "superresolved" temperature images with a nominal spatial resolution given by the infrared observations. Figure 1 illustrates how aliased, low-resolution observations can be used to reconstruct a superresolved estimate of the temperature field that optimally reproduces the statistical properties of the small scales.

It is important to emphasize that stochastic superresolution is not simply an image-processing technique; it is based upon an empirical stochastic model for the underlying turbulent dynamics that effectively parameterizes the unresolved eddies. The stochastic parameters appearing in the dynamical model are determined by regression fitting the model to reproduce the correct climatological temperature variance and temporal decorrelation times. Thus, the method uses statistical information about the small scales in conjunction with a model for how small-scale temperature features are aliased into the larger scales by coarse observations. Of course, as with other data assimilating and filtering approaches, stochastic superresolution does not create new information, but rather combines direct observations of large scales with fine-scale statistical information to produce an optimal estimate of the sea-surface temperature on small scales [*Wunsch*, 2006; *Majda and Harlim*, 2012]. The enhanced sea-surface temperature images can then be used to estimate upper ocean temperature and velocity statistics on kilometer scales.

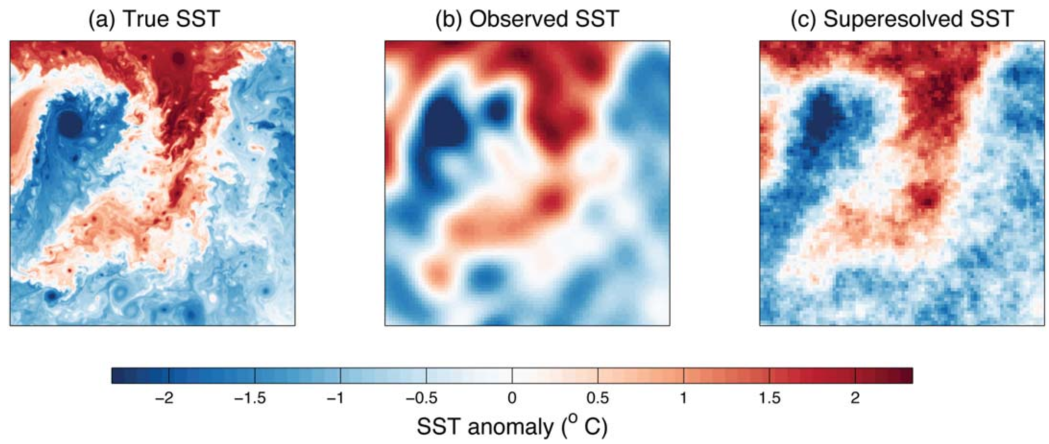

Figure 1. Snapshots of the sea-surface temperature (SST) anomaly in a 500 km × 500 km subregion of the Subtropical Pacific test case. From left: true, observed, and superresolved SST anomaly, in degrees Celsius. The low-resolution observation aliases small-scale features into large scales, while the superresolved estimate optimally reproduces the statistical properties of the unresolved scales.

The SQG method for inferring subsurface velocities from sea-surface temperature measurements is outlined in section 2. In section 3, we discuss in detail the procedure for deriving stochastic superresolved temperature images using statistical information about small scales. In section 4, we describe numerical simulations of baroclinically unstable ocean turbulence driven by climatological shear and stratification profiles for three contrasting regions at high, mid, and low latitudes that are used to test the technique in section 5. In section 6, the SQG method is applied using both superresolved and unprocessed observations of the simulations and compared with the results obtained using "perfect" observations of the surface temperature field. We summarize and discuss our results in section 7.

2. Surface Quasigeostrophic Method

In a geostrophically balanced flow, the stream function anomaly $\psi'(x,y,z)$ is fully determined by the interior potential vorticity and surface density anomalies,

$$q'(x,y,z)=\nabla^2\psi'+\frac{\partial}{\partial z}\left(\frac{f_0^2}{N^2}\frac{\partial\psi'}{\partial z}\right),\quad \rho'(x,y)=-\frac{f_0\rho_0}{g}\frac{\partial\psi'}{\partial z}(0), \tag{1}$$

where f_0 is the Coriolis parameter, ρ_0 is a reference density, and g is gravitational acceleration. In addition, there is the lower surface boundary condition $\partial_z\psi'=0$ on $z=-H$. Thus, if the interior potential vorticity and surface density anomalies are known, the interior stream function can be derived using the potential vorticity inversion principle [*Hoskins et al*., 1985]. *Isern-Fontanet et al*. [2008] found that, in much of the ocean, variations in surface density are dominated by the sea-surface temperature anomaly θ' so that $\rho' \approx -\rho_0 a_T\theta'$ where $a_T=0.15\times10^{-3}\,\mathrm{K}^{-1}$ is the thermal expansion coefficient for seawater. The surface boundary condition for the potential vorticity inversion is then

$$\theta'(x,y)=\frac{f_0}{ga_T}\frac{\partial\psi'}{\partial z}. \tag{2}$$

Lapeyre and Klein [2006] showed that, when surface dynamics dominate the upper ocean (the first few hundred meters), there is a robust correlation between the potential vorticity and sea-surface temperature anomalies,

$$q'(x,y,z)\approx\alpha(z)\theta'(x,y), \tag{3}$$

where $\alpha(z)$ is an empirically derived vertical profile function estimated from the large-scale meridional gradient of the potential vorticity, Q_y, and the surface temperature, T_y,

$$\alpha(z)=\frac{\langle Q_y(z)\,T_y\rangle_X}{\langle T_y^2\rangle_X}, \tag{4}$$

with $\langle\cdot\rangle_X$ representing a horizontal spatial average.

The profile function $\alpha(z)$ is easily estimated from hydrography and is remarkably effective at capturing the correlation between the potential vorticity and sea-surface temperature anomalies in the upper 500 m of the water column [*Lapeyre and Klein*, 2006]. This strong correlation means that individual observations of the sea-surface temperature can be used to derive the interior potential vorticity gradient and, by inverting (1), the subsurface horizontal velocity anomaly $\mathbf{u}'=\left(-\psi'_y, \psi'_x\right)$. In addition, the subsurface vertical velocity $w(x, y, z)$ can be derived by solving the omega equation [e.g., *Hoskins et al*., 1978],

$$f_0^2 w_{zz} - N^2(z)\nabla^2 w = -2f_0\nabla\cdot\mathbf{Q} + \beta f_0 v_z, \tag{5}$$

where $\mathbf{Q}=\left(u_x v_z - v_x u_z,\ u_y v_z - v_y u_z\right)$, and $u=U(z)+u'$ and $v=V(z)+v'$ include both the mean and perturbation velocities in the zonal and meridional directions, respectively.

As an illustrative example, consider the case when $\alpha(z)$ projects onto the first baroclinic mode, N is constant, and $H\to\infty$. The Fourier transform of the stream function $\hat{\psi}=\hat{\psi}_{kl}(z)$ is then,

$$\hat{\psi}(z) = -\frac{\alpha(z)\,\hat{\theta}}{K^2+K_1^2} + \frac{g a_T \hat{\theta}}{NK}\mathrm{e}^{NKz/f_0} \tag{6}$$

where $K=\left(k^2+l^2\right)^{1/2}$ is the isotropic horizontal wavenumber and K_1 is the first baroclinic wavenumber. The second term in (6) is a "surface mode" that ensures that the stream function satisfies the inhomogeneous boundary condition at the upper surface, namely $\psi_z(0)=(g a_T/f_0)\theta$. Thus, the stream function (6) is a smoothed version of the sea-surface temperature anomaly θ, since small scales (large K) will be suppressed by the K-dependent denominators. This motivates the need for higher-resolution sea-surface temperature images for use with the surface quasigestrophic method.

There are a number of additional caveats that limit the skill of the surface quasigeostrophic method in reconstructing the subsurface flow. The technique assumes that the surface density can be estimated from SST images alone, and, while this is appropriate in many regions of the ocean [*Isern-Fontanet et al*., 2008] this will not always be the case. The vertical profile function $\alpha(z)$ is calculated from hydrography and this might not accurately represent the correlation between the interior potential vorticity and SST anomalies in real time. Likewise, the presence of interior dynamics with little or no surface expression will lead to errors in the reconstruction. In this article, we compare the skill of the subsurface flow reconstructions estimated from SST images with both the true subsurface flow and the subsurface flow estimated from "perfect" observations of the SST. This latter case provides a useful benchmark with which to distinguish errors in the superresolved SST estimate and errors arising from the surface quasigeostrophic method itself.

3. Stochastic Superresolution of Sea-Surface Temperature Images

Majda and Grote [2007] and *Harlim and Majda* [2008] describe an efficient algorithm for estimating unresolved small-scale features from sparse, noisy observations of turbulent systems. The method exploits the fact that a low-resolution image will alias high-wavenumber modes into the resolved waveband. To illustrate this, consider the temperature field $\theta(x,y)$ evaluated on a high-resolution grid with grid spacing $\delta = L/N$, where L is the length of the domain and N is the number of grid points along each dimension. For simplicity, we will assume that the domain and observational grid are square and doubly periodic. Then the discrete Fourier transform on the high-resolution $N\times N$ grid is defined as

$$\hat{\theta}(k,l) = \frac{1}{N^2}\sum_{m,n=0}^{N-1}\theta(m\delta, n\delta)\,\mathrm{e}^{-2\pi\mathrm{i}(km+ln)/N}, \tag{7}$$

with nondimensional wavenumbers k, l taking integer values in ($-N/2$, $+N/2$]. By comparison, the same temperature field evaluated on a low-resolution $M\times M$ grid with grid spacing $\Delta = L/M$ has a discrete Fourier transform given by

$$\tilde{\theta}(k,l) = \frac{1}{M^2}\sum_{m,n=0}^{M-1}\theta(m\Delta, n\Delta)\,\mathrm{e}^{-2\pi\mathrm{i}(km+ln)/M}, \tag{8}$$

where now the nondimensional wavenumbers k, l take integer values in the narrower waveband ($-M/2$,

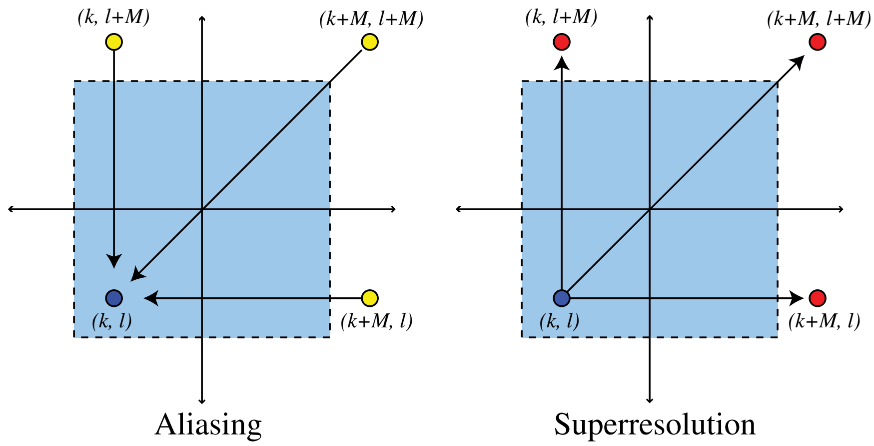

Figure 2. Spatial aliasing and superresolution in spectral space. (left) Wavenumber (k, l) (in blue) is observed on a low-resolution $M \times M$ grid with a resolved waveband indicated by the pale blue box. The observation will sample the resolved wavenumber (k, l) as well as aliased wavenumbers in the same aliasing set (in yellow). (right) An observation of the resolved wavenumber (k, l) is used to estimate the aliased modes (in red). When this is repeated for the entire resolved waveband, the resulting estimate has an effective resolution double that of the original observation in each direction.

$+M/2$]. Let us assume that $\Delta = P\delta$ where $P = N/M$ is an even integer. Then it is straightforward to show that the high-resolution and low-resolution Fourier transforms are related by

$$\tilde{\theta}(k,l) = \sum_{i,j=-P/2}^{P/2+1} \hat{\theta}(k+iM, l+jM) \tag{9}$$

That is, the low-resolution Fourier transform samples, with equal weight, all Fourier modes in the same aliasing set, i.e., that are aliased into the same resolved mode k, l (Figure 2).

More generally, an observation will sample the temperature over a footprint that can be described using a sampling weight $G(x, y)$,

$$\theta^{\mathrm{obs}}(x,y) = \int G(x',y')\, \theta(x-x', y-y')\, dx' dy'. \tag{10}$$

Here, $x = m\Delta$, $y = n\Delta$ for $m, n = 0, 1, \cdots M-1$ as before, while x', y' are allowed to vary over all space. By the convolution theorem (see Appendix A), the Fourier transform of the coarse observations is given by

$$\tilde{\theta}^{\mathrm{obs}}(k,l) = \sum_{i,j=-\infty}^{\infty} \hat{G}(k+iM, l+jM)\, \hat{\theta}(k+iM, l+jM), \tag{11}$$

where $\hat{\theta}$ now represents the continuous Fourier transform of the temperature field.

The spectral transfer function $\hat{G}$ is the Fourier transform of the sampling weight G. As a simple example, consider a Gaussian sampling weight of width ℓ. Then,

$$G(x,y) = \frac{1}{2\pi\ell^2} e^{-(x^2+y^2)/2\ell^2}, \quad \hat{G}(p,q) = e^{-2\pi^2(p^2+q^2)\ell^2/L^2}. \tag{12}$$

Thus, high-wavenumber aliased modes are weighted less than low-wavenumber modes, particularly for sampling weights with a wide footprint ($\ell \gg \Delta$). Conversely, for a narrow sampling footprint ($\ell \ll \Delta$), all aliased modes are weighted equally, $\hat{G} \approx 1$.

Spatial aliasing is often undesirable, especially when there is significant energy in the unresolved scales leading to a spurious modulation in the low-resolution image. Even so, the low-resolution image does contain information about the unresolved small scales in admixture with other wave modes. The problem of separating each resolved mode k, l from its aliases involves multiple unknowns and a single, integrated measurement (9). Underconstrained inverse problems of this kind arise frequently in oceanographic applications such as ocean acoustic tomography [*Munk et al.*, 1995], Lagrangian float trajectories [*Kuznetsov* *et al*., 2003], and satellite altimetry [*Keating et al*., 2012]. As in these examples, we adopt a two-step prediction–correction approach: (i) a forecast model makes a prediction of the full-system state at a future time, at which point (ii) an observation is made of some subset of the system and used to constrain (or correct) the prediction. The resulting updated estimate then forms the initial state for the next forecast step. An additional smoothing step (*iii*) can be retroactively applied to the entire time series to further optimize the state estimate. Below we describe how these steps are applied to derive superresolved sea-surface temperature images from low-resolution observations.

3.1. Forecast Step

Each complex-valued mode $\hat{\theta}=\hat{\theta}(k_i, l_j)$ is modeled as a Gaussian random variable governed by the linear stochastic differential equation

$$\partial_t\hat{\theta}=-(\gamma-\mathrm{i}\omega)\hat{\theta}(t)+\sigma\dot{W}(t), \tag{13}$$

where γ is a linear damping rate, ω is a linear frequency, and σ is a stochastic noise strength. The complex white noise forcing $\dot{W}=(\dot{W}_1+\mathrm{i}\dot{W}_2)/\sqrt{2}$ is defined in terms of independent real-valued white noise forcings $\dot{W}_n$ such that $\langle\dot{W}\rangle=\langle\dot{W}_n\rangle=0$ and $\langle|\dot{W}|^2\rangle=\langle\dot{W}_n^2\rangle=1$. Equation (13) is perhaps the simplest possible parameterization of a turbulent signal and has found wide application in turbulence modeling [*DelSole*, 2004; *Harlim and Majda*, 2010]. The Gaussianity of the initial state is preserved by the linear stochastic model, so the predicted state is determined solely by the predicted mean $\langle\hat{\theta}\rangle$ and covariances $\langle\hat{\theta}_p\hat{\theta}_q^*\rangle$, which can be calculated analytically from (13).

The stochastic parameters γ, ω, and σ are determined offline mode-by-mode by tuning (13) to reproduce the correct time-mean temperature variance $\Theta=\langle\hat{\theta}^2\rangle$ and the first-crossing time and e-folding time of the autocorrelation function $R(\tau)=\Theta^{-1}\langle\hat{\theta}(t)\hat{\theta}^*(t+\tau)\rangle$. For the linear stochastic model (13),

$$\Theta=\frac{\sigma^2}{2\gamma}, \qquad R(\tau)=\mathrm{e}^{-\gamma\tau}(\cos\omega\tau+\mathrm{i}\sin\omega\tau), \tag{14}$$

so the first-crossing time is $\pi/2\omega$ and the e-folding time is $1/\gamma$.

Because the forecast model (13) generates a prediction for each mode on the high-resolution $N\times N$ grid, the stochastic parameters γ, ω, σ must also be estimated using high-resolution observations, i.e., infrared temperature images. Since these parameters only depend upon the statistics of the small scales (the temperature variance and correlation function), they will not be very sensitive to occasional data outages from cloud cover, as we shall demonstrate.

3.2. Update Step

The forecast model (13) generates a prediction for the temperature on the high-resolution $N\times N$ grid at a future time. At this point, an observation is made on the low-resolution $M\times M$ grid. For each resolved mode $\tilde{\theta}=\tilde{\theta}(k,l)$, the observation returns a sum over the aliasing set of k, l plus some observational noise $\tilde{n}=\tilde{n}(k,l)$,

$$\tilde{\theta}=\mathrm{G}\hat{\theta}+\tilde{n}, \qquad \hat{\theta}=\{\hat{\theta}(k+iM, l+jM)\} \tag{15}$$

where G is the $P^2\times1$ observation operator representing the weighted sample (10) and $\hat{\theta}$ is the $1\times P^2$ vector of modes aliased into k, l. In this article, we will consider the simplest case of $\mathrm{G}=\{1,1,\cdots1\}$, which is equivalent to assuming a small sampling footprint ($\ell\ll\Delta$) in (10). However, the method proceeds in exactly the same manner if this assumption is relaxed and a broader sampling footprint is considered.

Notice that, although the observation couples all modes in the same aliasing set, each set is disjoint. Thus, if the aliasing sets are initially uncorrelated, they will remain so under the action of the forecast model (13) and the observation operator (15). This leads to a dramatic simplification of the full N^2-dimensional inverse problem, allowing us instead to deal with separate P^2-dimensional inverse problems for each of the $M\times M$ resolved modes [*Harlim and Majda*, 2008]. If $P=2$, for example, this means that we only need to calculate the inverse of M^2 different 4×4 covariance tensors instead of a single $4M^2\times4M^2$ covariance tensor, a significant reduction in the computational overhead.

The inverse problem can then be stated as finding the optimal state estimate $\hat{\theta}_+$ given the forecast $\hat{\theta}_-$ and the observation $\tilde{\theta}$. A compelling advantage of the idealized linear stochastic forecast model (13) is that the optimal estimate is provided by the *Kalman* [1960] filtering solution: the forecast and observation are Gaussian random variables with mean $\langle\hat{\theta}_-\rangle$ and $\langle\tilde{\theta}\rangle$ and covariance R_- and R_o, so the updated state estimate is also a Gaussian random variable with mean and covariance satisfying

$$\langle\hat{\theta}_+\rangle=(\mathsf{I}-\mathsf{KG})\langle\hat{\theta}_-\rangle+\mathsf{K}\tilde{\theta}, \qquad \mathsf{R}_+=(\mathsf{I}-\mathsf{KG})\mathsf{R}_-, \tag{16}$$

where $\mathsf{K}=\mathsf{R}_-\mathsf{G}^T\left(\mathsf{GR}_-\mathsf{G}^T+R_o\right)^{-1}$ is the Kalman gain matrix [e.g., *Wunsch*, 2006; *Majda and Harlim*, 2012]. The updated state estimate is then used as the initial state for the next forecast step.

3.3. Smoothing Step

The Kalman filter will generate the optimal estimate of the current temperature field given all observations up to that point. However, this results in a time series that can have unphysical jumps in the state estimate. In the present application, an additional Kalman smoothing operation is applied after the Kalman filter has been run forward through the time series that further optimizes the temperature estimate at every time step. We use the efficient *Rauch et al*. [1965] smoother to calculate the mean $\langle\hat{\theta}_s\rangle$ and covariance R_s of the smoothed state estimate. The calculation proceeds backward in time using the recursive relations,

$$\begin{aligned}\langle\hat{\theta}_s\rangle(t)&=\langle\hat{\theta}_+\rangle(t)+\mathsf{H}(t)[\langle\hat{\theta}_s\rangle(t+\Delta t)-\langle\hat{\theta}_-\rangle(t+\Delta t)],\\ \mathsf{R}_s(t)&=\mathsf{R}_+(t)+\mathsf{H}(t)[\mathsf{R}_s(t+\Delta t)-\mathsf{R}_-(t+\Delta t)]\mathsf{H}^*(t),\end{aligned} \tag{17}$$

where $\mathsf{D}=\mathrm{diag}(\exp[-(\gamma+i\omega)\Delta t])$ and $\mathsf{H}(t)=\mathsf{R}_+(t)\mathsf{DR}_-^{-1}(t+\Delta t)$.

Note that the end result of this process—the smoothed state estimate—is a Gaussian random variable characterized by its mean and covariance with a nominal resolution equal to that of the infrared observations. We will refer to this as the *superresolved estimate*.

4. Numerical Simulations

We test the method using quasigeostrophic simulations forced by mean shear and stratification profiles obtained from the Ocean Comprehensible Atlas [*Forget*, 2010]. This 3 year climatology for the period December 2003 to November 2006 assimilates altimeter, sea-surface temperature, and Argo float data using the adjoint of the MITgcm [*Marshall et al*., 1997]. The resulting hydrographic data are available on a $1^\circ\times1^\circ$ grid with 50 vertical levels.

Figure 3 shows the zonal and meridional velocity profiles for three regions characterized by strong fronts and eddies on scales of 10–50 km: (i) the Antarctic Circumpolar Current (101°W 58°S), (ii) the Gulf Stream (68°W 38°N), and (iii) the Subtropical Pacific (154°E 23°N). In the Antarctic Circumpolar Current (ACC), the flow is dominantly zonal with a deep, baroclinic mode-1 structure, and strong shear throughout the upper ocean. This region, which is the subject of a field campaign to study diapycnal and isopycnal mixing in the Southern Ocean [DIMES; *Sheen et al*., 2013], exhibits sharp fronts and relatively small deformation scales that are challenging to observe using altimetry. The velocity profile in the Gulf Stream region is also sheared throughout the upper 500 m due to strong lateral density gradients associated with the convergence of subtropical and subpolar waters. The recent Lateral Mixing field campaign [LatMix; *Shcherbina et al*., 2013] has targeted this region to study eddy mixing on submesoscales (100 m–10 km). The third region, the western Subtropical Pacific, has strong stratification and a shallow pool of potential vorticity with negative meridional gradient beneath an eastward surface current. Flows of this kind are susceptible to small-scale Charney instability near the surface with large variance in the temperature field at small scales [*Tulloch et al*., 2011; *Roullet et al*., 2012].

The numerical model evolves the quasigeostrophic potential vorticity,

$$\frac{\partial q}{\partial t}+\mathbf{u}\cdot\nabla q=\mathcal{D}(\mathbf{u}), \quad q=f(y)+\nabla^2\psi+\frac{\partial}{\partial z}\left(\frac{f^2}{N^2(z)}\frac{\partial\psi}{\partial z}\right) \tag{18}$$

where $\psi=V(z)x-U(z)y+\psi'$ is the perturbed geostrophic stream function, $\mathbf{u}'=\left(-\psi'_y,\psi'_x\right)$ is the horizontal velocity anomaly, and $f(y)=f_0+\beta y$ is the Coriolis parameter. A quadratic drag $\mathcal{D}(\mathbf{u})=-C_d h^{-1}(\partial_x|\mathbf{u}|v-\partial_y|\mathbf{u}|u)\delta(z+H)$ acts on the bottom boundary at $z=-H$, where C_d is the quadratic drag coefficient and h is the bottom boundary layer thickness.

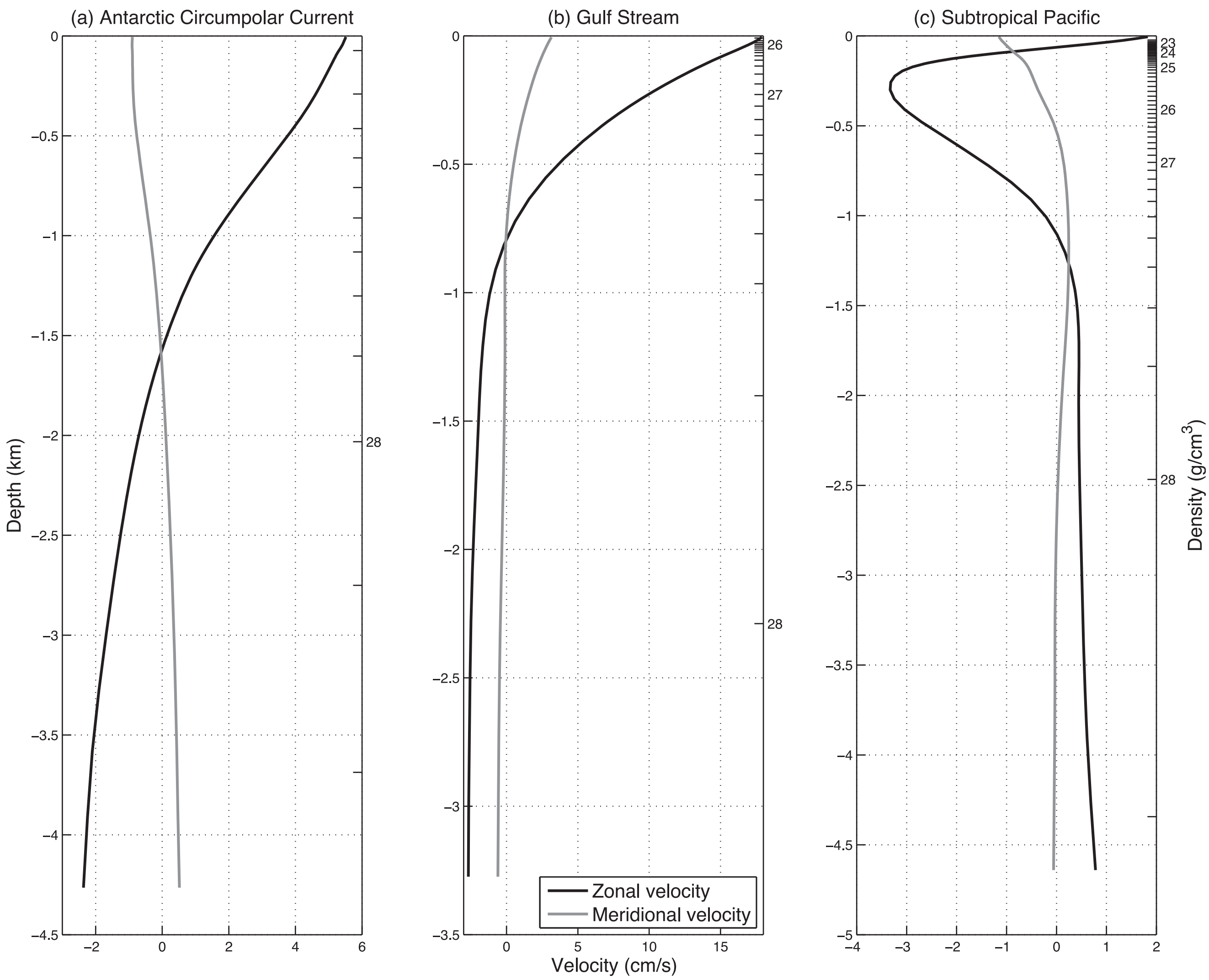

Figure 3. Zonal and meridional velocity profiles from the *Forget* [2010] hydrographic atlas: (a) Antarctic Circumpolar Current (101°W 58°S), (b) Gulf Stream (68°W 38°N), (c) Subtropical Pacific (154°E 23°N). Isopycnal depths in increments of 0.1 g/cm^3 are shown on the right-hand axes.

Equations (18) were solved numerically on a horizontally periodic domain using a leap-frog time-stepping scheme with a Robert-Asselin filter, finite-differencing in the vertical, and a dealiased, pseudo-spectral method to compute the nonlinear terms. The vertical grid-spacing was chosen to match the *Forget* [2010] hydrographic data (up to 50 vertical levels) and the horizontal grid was 1024 × 1024, corresponding to a horizontal grid spacing of less than 1.5 km. The quadratic drag coefficient $C_d = 3 \times 10^{-3}$ and the bottom turbulent boundary layer thickness $h = 50$ m. An additional exponential filter dissipated enstrophy on small scales. The model parameters for each test region are shown in Table 1.

5. Sea-Surface Temperature Reconstruction

Daily synthetic sea-surface temperature observations were generated over a 90 day period for each test region with both infrared and microwave resolutions, or approximately 5 km ($N = 256$) and 40 km ($M = 32$), respectively (Table 1). The high-resolution observations were used to estimate the model parameters in the empirical forecast model (13), while the low-resolution observations provided the input data stream for the Kalman filter. Observational noise was distributed uniformly across all Fourier modes, so the observational error covariance matrix for each aliasing set was diagonal. The total observational error covariance was 10% of the time-mean temperature variance. For each observed wavenumber, the resolved mode plus seven

Table 1. Model Parameters for Test Regions

Region Name	ACC	Gulf Stream	Subtropical Pacific
Location	101°W 58°S	68°W 38°N	154°E 23°N
Domain depth	4446 m	3422 m	4834 m
Domain length	1352 km	1298 km	1473 km
Deformation radius	56 km	65 km	184 km
Observation grid size	42 km	41 km	46 km
Superresolved grid size	5.3 km	5.1 km	5.8 km

aliased modes in each direction were filtered, so that $8 \times 8 = 64$ modes were filtered per observed mode. The resulting superresolved estimate of the sea-surface temperature field therefore has a nominal resolution eight times that of the original microwave observations.

Snapshots of the true, observed, and superresolved estimates of the sea-surface temperature field for one of the test cases, the Subtropical Pacific, are shown in Figure 1. Note that the superresolved estimate is actually a single realization of a Gaussian random field, generated using the mean and noise covariance of the smoothed state estimate. This accounts for its noisy appearance. The superresolved estimate does not resolve all of the small-scale features, but it does capture the statistics of the unresolved scales. This is particularly notable in the lower left-hand corner of the image, where several small eddies are aliased into a large eddy by the observations. The superresolved estimates reproduce the approximate scales and energies of these eddies. The superresolved estimate also recreates the convoluted front between the warm and cold regions of the flow that are otherwise smoothed out by the raw observation.

Figure 4 compares time series of the true, observed, and superresolved temperature anomaly for a single-resolved wavenumber and the first three modes in the same aliasing set. This particular wavenumber $(-16,15)$ lies near the edge of the resolved waveband $-16 \leq k,l \leq 16$ and so has an amplitude similar to that of its aliases. This means that the observations (black circles) are not dominated by any one mode and are strikingly different from the true temperature anomaly at that wavenumber. Even so, the filter produces an estimate of the mean (solid gray line) and standard deviation (gray-shaded region) of both the resolved

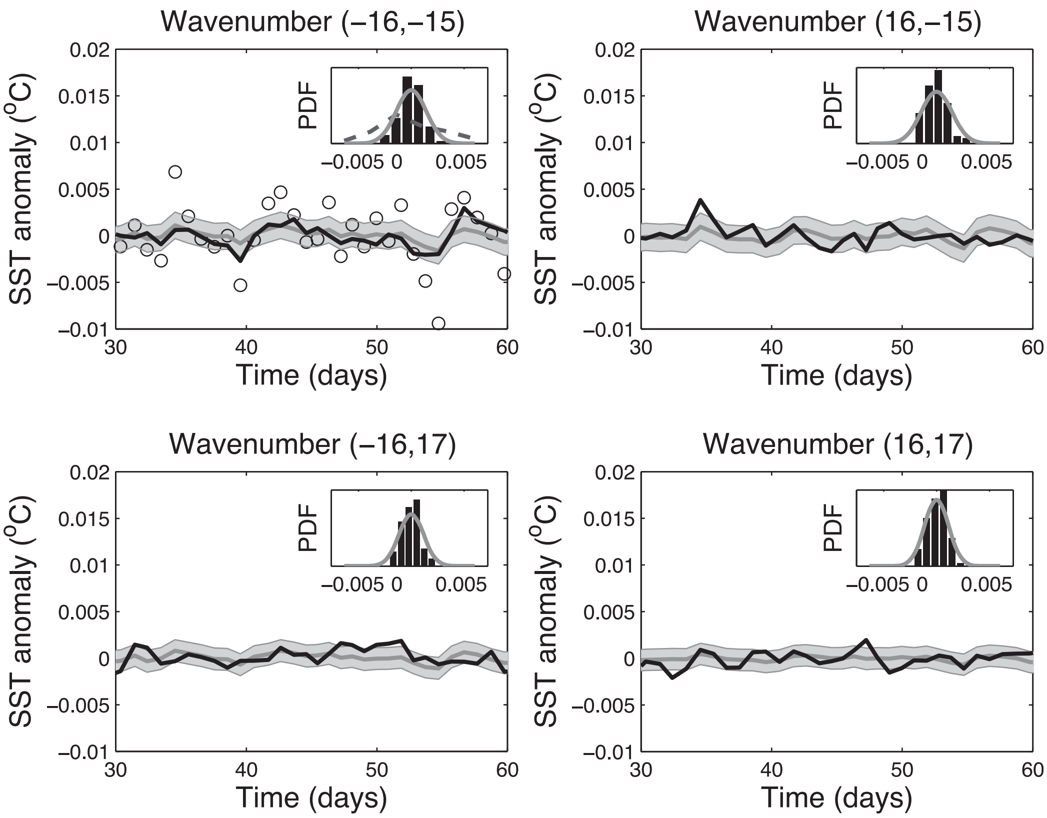

Figure 4. Time series of the true (black line), observed (black circles), and superresolved (gray band) estimate of the sea-surface temperature anomaly in the Antarctic Circumpolar Current region. Shown are the real parts of the Fourier components for resolved wavenumber $(-16,-15)$ and the first three aliased modes in the same aliasing set: $(16,-15)$, $(-16,17)$, and $(16,17)$. Observations are available only for the resolved mode. The shaded region shows one standard deviation about the (smoothed) superresolved estimate. The inset figures show the PDF of the true (black bars), observed (dashed gray curve), and superresolved (solid gray curve) fields.

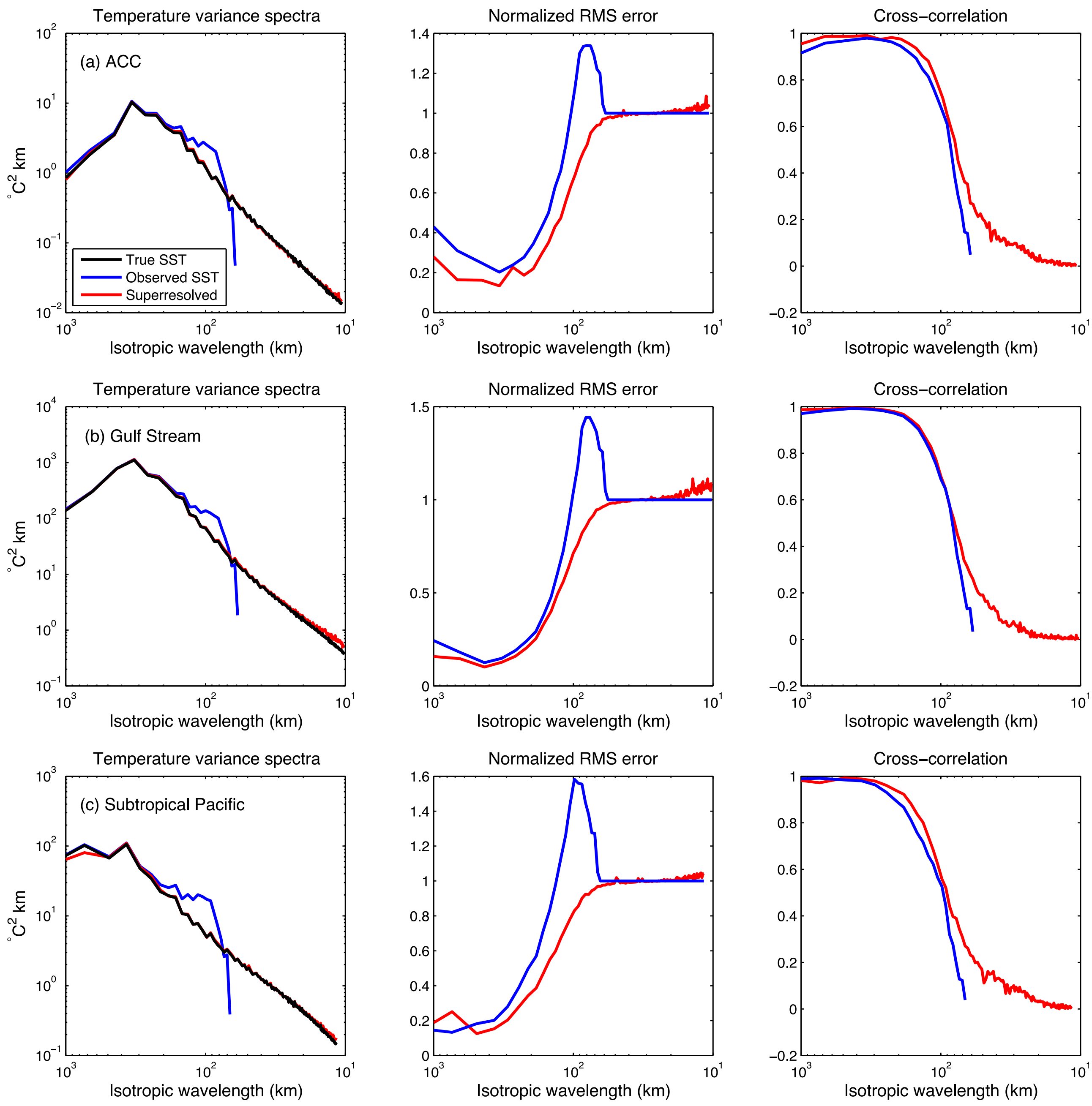

Figure 5. Temperature variance spectra, normalized RMS error, and cross-correlation for (a) Antarctic Circumpolar Current (ACC), (b) Gulf Stream, and (c) Subtropical Pacific.

and unresolved modes that accurately reconstructs the energy and even some of the temporal variability of the signal. This is also apparent in the PDFs of the sea-surface temperature estimates, shown in the inset graphs in Figure 4 (measured with respect to a 7 day moving window average). The observations do a poor job of capturing the mean and variance of the true sea-surface temperature PDF of the resolved mode $(-16,-15)$ and are not available at all for the unresolved modes. By contrast, the superresolved estimates are able to reproduce the PDF of both resolved and unresolved modes.

The skill of the filter in reconstructing the sea-surface temperature at each isotropic wavenumber is measured in Figure 5 using the temperature variance spectra, RMS error (normalized by the true temperature variance at that wavenumber), and cross-correlation,

$$\mathrm{RMSE}(K)=\sqrt{\frac{\langle|\hat{\theta}_{est}-\hat{\theta}|^2\rangle_K}{\langle|\hat{\theta}|^2\rangle_K}}, \tag{19}$$

$$\mathrm{XCORR}(K)=\frac{\langle\hat{\theta}_{est}\hat{\theta}\rangle_K}{\sqrt{\langle|\hat{\theta}_{est}|^2\rangle_K\langle|\hat{\theta}|^2\rangle_K}}. \tag{20}$$

where $\hat{\theta}_{est}$ is the observed or superresolved temperature estimate and $\langle\cdot\rangle_K$ are averages over all wavenumbers satisfying $k^2+l^2=K^2$. To facilitate comparison, the observations were interpolated to the same resolution as the superresolved estimate by padding the Fourier transform with zeros. The observations tend to overestimate the temperature variance near the limit of resolution (approximately 40 km) due to the effect of aliasing of unresolved modes, while the superresolved estimate correctly redistributes this energy to small scales. The superresolved sea-surface temperature has consistently lower RMS error and higher cross correlation than the observations. In particular, the effect of spatial aliasing near the limit of resolution results in a peak in the RMS error in the observation that is absent in the superresolved estimate. At very small scales, the RMS error of the observed and superresolved estimates tend to one because the magnitude of $\hat{\theta}_{est}$ becomes very small.

In principle, the accuracy of the small-scale statistics (temperature variance and correlation function) calculated using the high-resolution observations can be impacted by clouds or the observing period of the infrared observations. To test the filter performance with intermittently cloudy observations, we modeled the effect of clouds by discarding a random selection of frames (between 0% and 90%). These frames were then substituted with images generated by linearly interpolating between neighboring cloud-free frames. Likewise, the length of the observing period used to calculate the small-scale statistics was varied between 10 and 90 days. In each case, the resulting series of daily high-resolution sea-surface temperature observations was used to calculate the empirical stochastic model parameters and the filter was applied as before to the entire 90 day interval of daily coarse-resolution observations. Figure 6 shows the total RMS error versus the fraction of cloud-free days and the length of the observing period for the Antarctic Circumpolar Current test case. (Results for the other two test cases are essentially the same.) The filter skill is found to be relatively insensitive to both clouds and observing period as long as roughly 25 days of cloud-free observations are available to train the empirical stochastic model. Filter skill for both the observed and superresolved estimates improves with observing time, perhaps due to more accurate estimate of the time-mean temperature field.

6. Subsurface Flow Estimation

The SQG method described in section 2 and its variants rely upon the strong correlation of the surface density (or temperature) with the interior potential vorticity. Clearly this will only be valid to a certain depth that will vary regionally. This is illustrated in Figure 7, which shows the time-averaged potential enstrophy

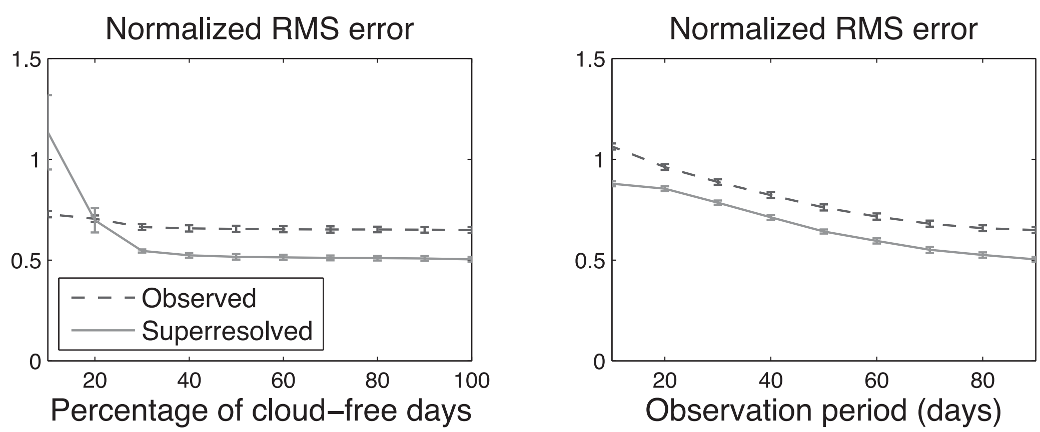

Figure 6. Total RMS error (normalized by total temperature variance) versus fraction of cloud-free days (left) and length of observing period for Antarctic Circumpolar Current test case. Error bars show one standard deviation.

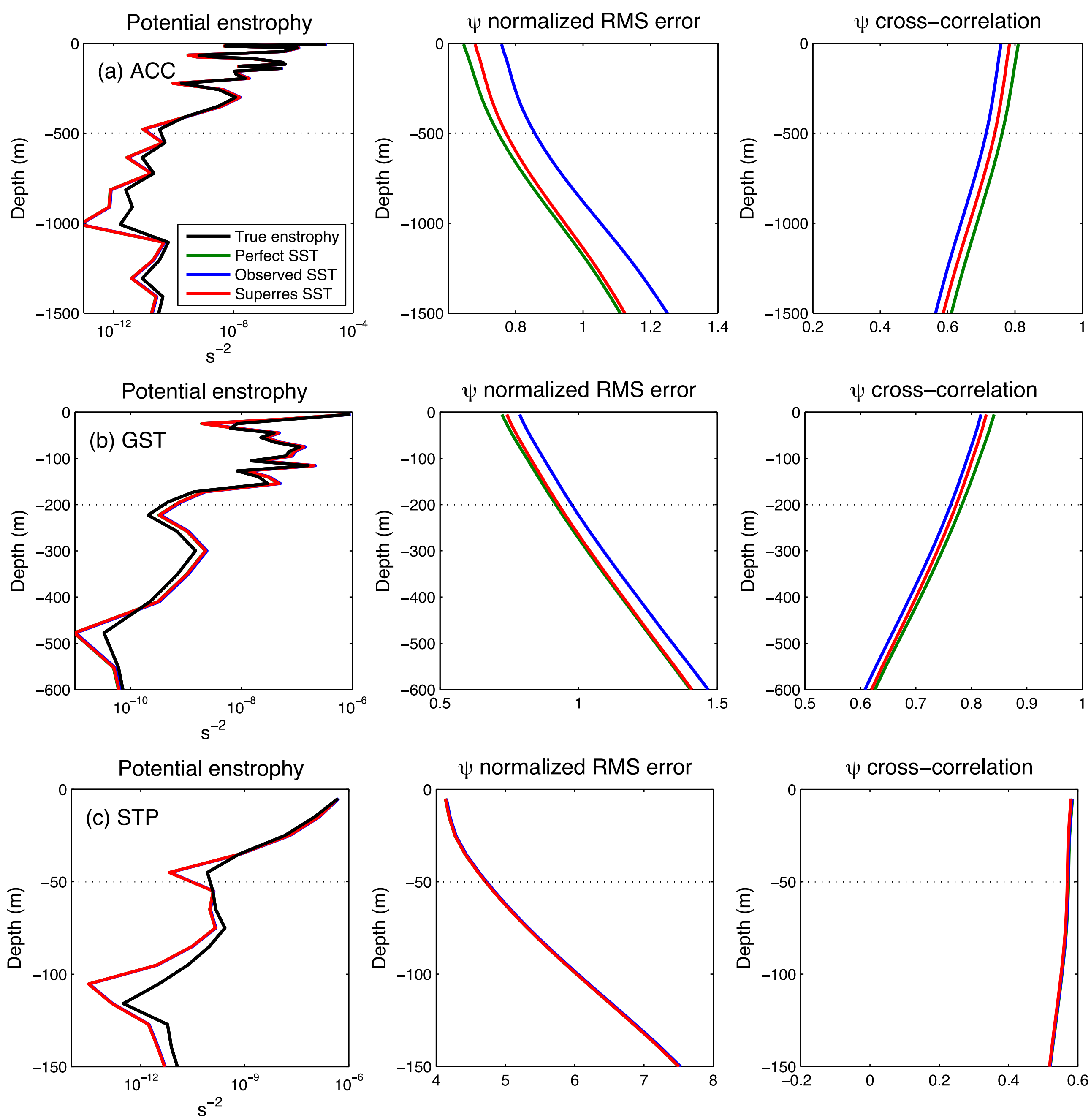

Figure 7. (left column) Potential enstrophy profiles for the three test regions: (a) Antarctic Circumpolar Current (ACC), (b) Gulf Stream (GST), and (c) Subtropical Pacific (STP). Also shown is the potential enstrophy profile estimated using the SQG method using "perfect" observations of the SST field (green) as well as the low-resolution (microwave) observations (blue) and the superresolved SST field (red). (middle column) Normalized RMS error for the reconstructed stream functions. (right column) Cross correlation for the reconstructed stream function.

profile $\langle |q|^2 \rangle/2$ calculated using the true stream function, compared with the potential enstrophy estimated from (3) using high-resolution ("perfect") SST observations, the low-resolution (microwave) SST observations, and the superresolved SST estimate. In each region, the potential enstrophy profile estimated by projecting the three SST observations are very similar at all depths (they are essentially superimposed in Figure 7) because they use the same empirical vertical profile $\alpha(z)$ to project the SST to depth; however, they differ from the true potential enstrophy in all regions. In the Antarctic Circumpolar Current test case, the projected SQG estimate closely matches the true potential enstrophy down to depths of up to 700 m. In the Gulf Stream and Subtropical Pacific test cases, the skill of the SQG method decreases much more rapidly with depth. (Notice the different vertical scales in each panel.) Even with perfect observations of the SST, the

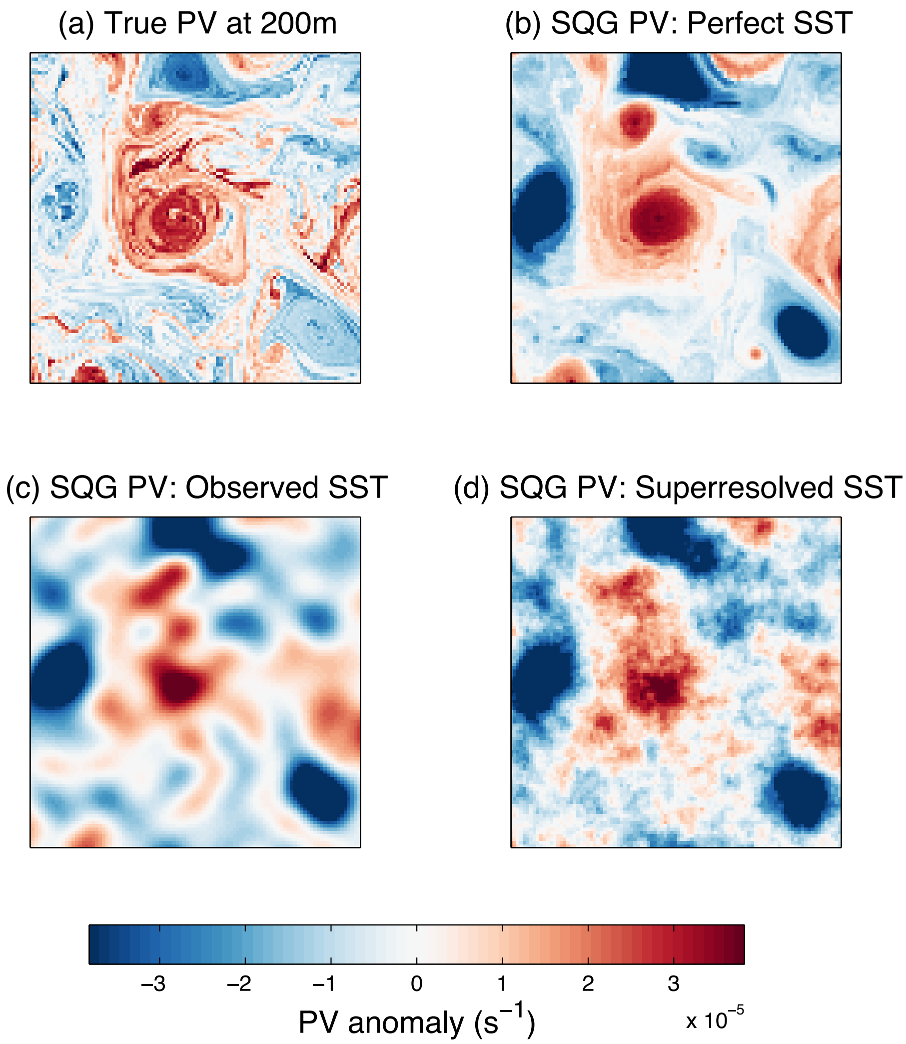

Figure 8. Snapshots of the potential vorticity (PV) anomaly at 200 m in a 500 km × 500 km subregion of the Gulf Stream test case: (a) true PV anomaly, (b) PV anomaly estimated using the SQG projection of "perfect" SST observations, (c) PV anomaly estimated using low-resolution (microwave) SST observations, (d) PV anomaly estimated using superresolved SST observations.

stream function estimate loses accuracy around 500 m in the Gulf Stream and around 100 m in the Subtropical Pacific.

Snapshots of the true and estimated potential vorticity anomaly at 200 m in the Gulf Stream test case are shown in Figure 8. The SQG estimates capture the dominant positive-PV anomaly at the center of the snapshot, because this feature has a large vertical extent. However, the surrounding negative-PV anomalies seen in each of the SQG estimates are much weaker than is the case for the true PV snapshot.

We found that the SQG method tended to overestimate the depth to which surface features extended, particularly in the Gulf Stream and Subtropical test cases, where surface dynamics are dominated by strong shear in the upper few hundred meters. By comparison, in the Antarctic Circumpolar Current, the water column is weakly stratified and the flow is dominated by a deep first baroclinic vertical mode that closely matches the SQG mode.

Using the estimated potential vorticity field, (1) is then inverted to calculate the subsurface stream function. Details of the kinetic energy spectra, normalized RMS error, and cross correlation for the estimated horizontal stream function ψ are shown in Figure 9, at 500, 200, and 50 m for the Antarctic Circumpolar Current, Gulf Stream, and Subtropical Pacific regions, respectively. These depths are indicated by the horizontal-dashed lines in Figure 7 for reference. The SQG estimates predict too much energy at large scales in all regions. This is particularly striking in the Subtropical Pacific case, where the true KE drops quickly with

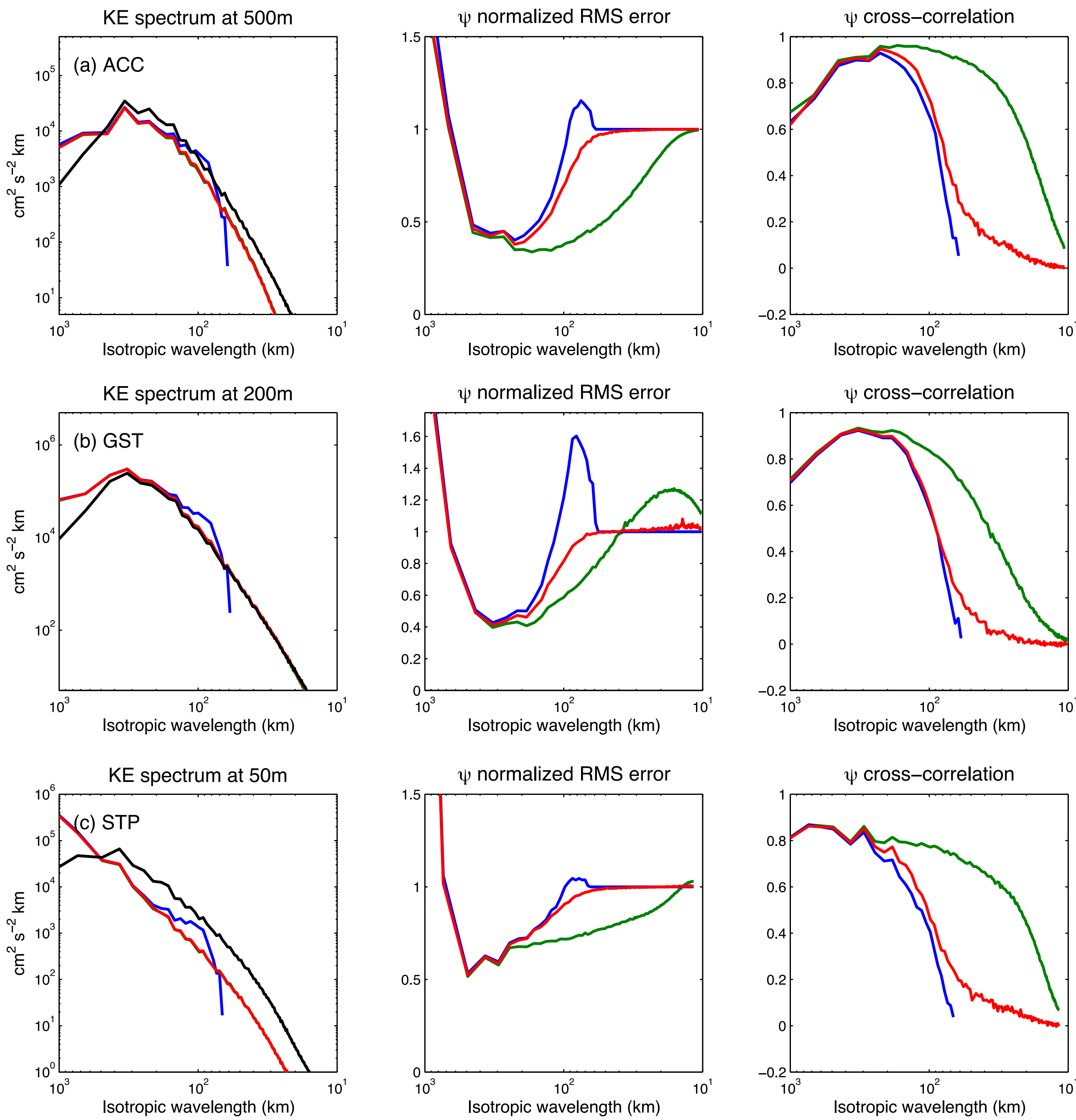

Figure 9. Kinetic energy spectra, normalized RMS error, and cross correlation for the true and estimated horizontal stream function, for each of the test regions.

depth compared with the SQG estimates. We suspect that this is due to the fact that at low *K*, the surface mode is very close to barotropic, resulting in too much large-scale energy at depth. Even so, in all three regions, the superresolved SST field results in an estimate of the kinetic energy at depth that is as good as that obtained using the true SST. However, the RMS error and cross correlation of the perfect SST observations is typically better than the superresolved estimate at small scales. This is because, although the superresolved estimate correctly redistributes aliased energy to small scales, it does so in a random, noisy way.

The noisy nature of the superresolved estimate of the subsurface stream function strongly impacts the vertical velocity estimated from the omega equation (5). We found little skill in reconstructing the vertical velocity field at depth in the Antarctic Circumpolar Current region (Figure 10) and none at all in the

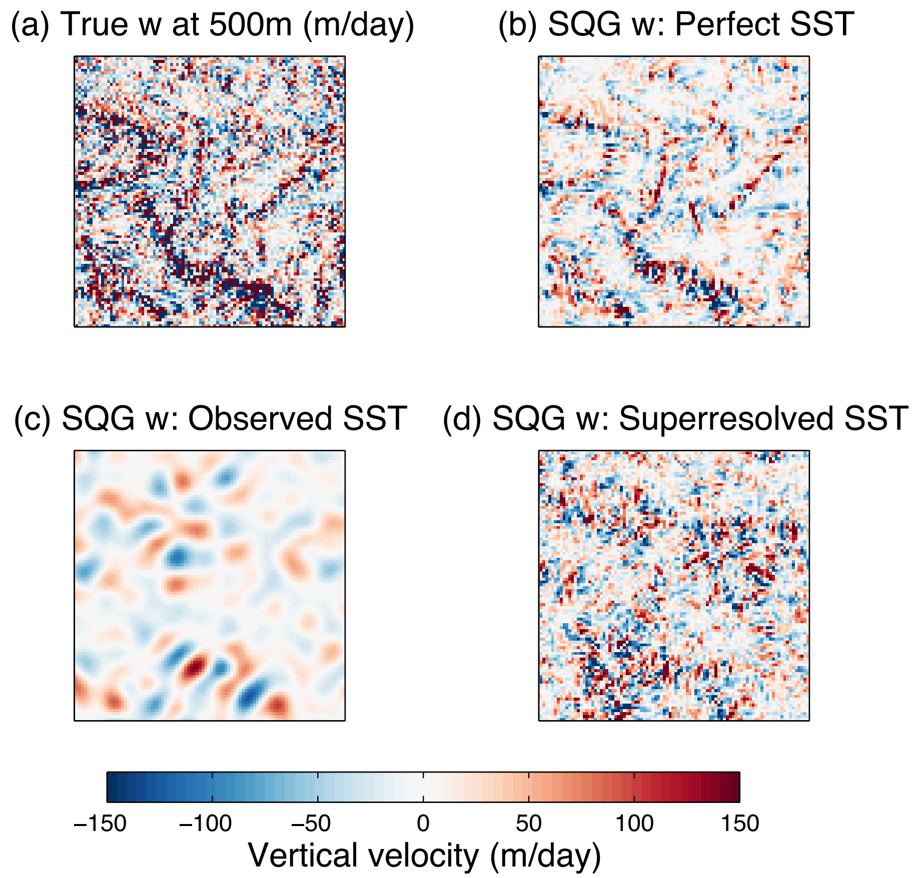

Figure 10. Snapshots of the vertical velocity at 500 m in a 500 km × 500 km subregion of the Antarctic Circumpolar Current test case: (a) true vertical velocity, (b) vertical velocity estimated using "perfect" SST observations, (c) vertical velocity estimated using low-resolution (microwave) SST observations, (d) vertical velocity estimated using superresolved SST observations.

Gulf Stream and Subtropical Pacific (not shown). One reason for this is that the true vertical velocity field is very fine scale and is organized along filaments and fronts in the temperature field [*Roullet et al*., 2012]. This makes the subsurface vertical velocity field extremely difficult to estimate using low-resolution surface temperature observations. Even with perfect SST observations, only the broad features of vertical velocity field are captured using the SQG method. The superresolved estimate produces the correct scales and magnitudes for the vertical velocity field, but is unable to reproduce the overall structure. By comparison, the unfiltered observations are completely unable to estimate the vertical velocity field. In the Gulf Stream and Subtropical Pacific cases, the SQG method fails, even with perfect observations of the sea-surface temperature field. Again, this is possibly due to a decoupling between the surface dynamics and the interior flow at depth for these regions. In all cases, the stream function estimated from superresolved SST images results in vertical velocities estimates that are dominated by small-scale noise, and so should be viewed as unreliable.

7. Conclusions

In this article, we have described a method for combining low-resolution (but cloud-penetrating) microwave temperature observations with an empirical model for the small scales derived from high-resolution (but intermittently cloudy) infrared measurements. The method, *stochastic superresolution*, extracts information about "unresolved" scales that nonetheless project some energy onto the resolved wave modes due to the effect of spatial aliasing. The resulting temperature estimates, which have a nominal resolution given by the underlying empirical model rather than the observations. These are then used to estimate the velocity field in the upper ocean on scales of 30–100 km using the surface quasigeostrophic method of *Lapeyre and Klein* [2006].

The method is tested in quasigeostrophic simulations of three regions with strongly contrasting dynamics: the Antarctic Circumpolar Current, the Gulf Stream, and the western Subtropical Pacific. All of these regions are characterized by strong fronts and eddies on scales of 10–50 km, though for different dynamical reasons. In the case of the Antarctic Circumpolar Current, the deformation wavelength is O(50 km) but the corresponding vertical scales extend to 1000 m. In the Gulf Stream and Subtropical Pacific regions, the small-scale flow features are generated by frontal dynamics and Charney-type instabilities that have a much shallower vertical extent and do not necessarily reflect the interior dynamics.

This regional variation has a strong impact on the depth to which the SQG mode can be projected, even with perfect observations of the sea-surface temperature field. In the Antarctic Circumpolar Current, the superresolved temperature estimate results in reasonably good subsurface flow reconstruction down to depths of up to 1000 m, whereas in the Gulf Stream and Subtropical Pacific the method loses accuracy at roughly 300 and 100 m, respectively. When compared with the subsurface flow estimated using the raw temperature observations, the superresolved temperature effectively reconstructs the statistics of features on smaller horizontal and vertical scales. This is particularly notable near the edge of the resolved waveband (approximately 40 km), where spatial aliasing has a strong effect on the observed signal.

Clearly, this is a limitation of the SQG projection itself and is present even with perfect observations of the sea-surface temperature. As such, the performance of the SQG method in the Gulf Stream and Subtropical Pacific regions argues strongly for the inclusion of additional barotropic or baroclinic modes to model the interior dynamics [*Lapeyre*, 2009; *Wang et al*., 2013] or a new basis set incorporating both surface and interior effects [*Smith and Vanneste*, 2013]. This is beyond scope of this study, however. Within the domain of validity of the SQG method, we find that the superresolved sea-surface temperature estimate results in consistently more accurate upper ocean stream function reconstruction when compared with the raw observations. This is particularly striking at wavenumbers close to the limit of resolution, where the effect of spatial aliasing gives rise to spurious energy at those wavenumbers. Since the SQG mode projects SST anomalies to a depth that depends upon wavenumber, spatial aliasing in the horizontal results in surface features that are overextended in the vertical. Stochastic superresolution effectively corrects this issue by accurately redistributing this energy to smaller horizontal—and vertical—scales.

The use of stochastic superresolution is not limited to sea-surface temperature observations. The method has already been applied to satellite altimetry [*Keating et al*., 2012] and we anticipate that the method could profitably be applied to satellite observations of other oceanic variables such as salinity or chlorophyll. The performance of the filter is contingent on two requirements: first, that significant variance is present at unresolved scales resulting in an aliased signal in the resolved wave band, and second that a forecast model can be derived for the unresolved scales. In the present case, high-resolution infrared observations were used to derive the parameters in the stochastic forecast model, which had the advantage that it was insensitive to intermittent clouds. Moreover, the forecast model itself was "dynamics-free", in that it did not rely on an a priori model for the temperature field but instead derived it empirically. In the more general framework, the forecast model could be based upon some reduced mean-field representation of the unresolved scales. Alternatively, the stochastic model parameters could be learned adaptively from the observations themselves [*Harlim and Majda*, 2010; *Majda and Harlim*, 2012]. These extensions will be taken up in future studies.

In this article, we have described a method for using superresolved SST images to reconstruct the features in the upper ocean on scales below the resolution of current-generation satellite altimeters. These scales are of critical importance for resolving outstanding questions about the transport pathways, biogeochemistry, and climate sensitivity of the ocean. It is hoped that this work will contribute toward our understanding of these scales and to the design of planned wide-swath satellite altimetry missions (SWOT, COMPIRA) as well as the next generation of high-resolution ocean climate models.

Appendix A : Spectral Transfer Function

We provide here the derivation of (11) in one dimension; the extension to two dimensions is straightforward. The discrete Fourier transform of the coarse observation (10) is

$$\tilde{\theta}^{\text{obs}}(k)=\frac{1}{M}\sum_{m=0}^{M-1}\int_{-L}^{L} G(x')\theta(x_m-x')e^{-2\pi i k x_m/L}\,dx', \tag{A1}$$

where $x_m=mL/M, m=0,1,\cdots M-1$ are the observation grid points. The true temperature field can be expressed in terms of its continuous Fourier transform via

$$\theta(x)=\int_{\infty}^{-\infty}\hat{\theta}(p)e^{2\pi i p x/L}\,dp. \tag{A2}$$

The nondimensional wavenumber p will be aliased into resolved wavenumbers p' in (–$M/2$, $M/2$] if $p=p'+jM$ for any integer j. Therefore, we can rewrite (A2) as

$$\theta(x)=\sum_{j=-\infty}^{\infty}\int_{-M/2}^{M/2}\hat{\theta}(p'+jM)e^{2\pi i(p'+jM)x/L}\,dp'. \tag{A3}$$

If we now introduce the spectral transfer function

$$\hat{G}(p)=\int_{-L}^{L}G(x')e^{-2\pi i p x'/L}dx', \tag{A4}$$

then (A1) becomes

$$\tilde{\theta}^{\text{obs}}(k)=\frac{1}{M}\sum_{m=0}^{M-1}\sum_{j=-\infty}^{\infty}\int_{-M/2}^{M/2}\hat{G}(p'+jM)\hat{\theta}(p'+jM)e^{2\pi i(p'-k)m/M}dp', \tag{A5}$$

where we have used the fact that $e^{2\pi ijm}=1$ for integers j and m. Finally, we make use of the identity $\sum_m e^{2\pi i(p'-k)m/M}=M\delta(p'-k)$ to obtain

$$\tilde{\theta}^{\text{obs}}(k)=\sum_{j=-\infty}^{\infty}\hat{G}(k+jM)\hat{\theta}(k+jM). \tag{A6}$$

This is the one-dimensional analogue of equation (11).

Acknowledgments
This work has benefitted greatly from discussions with Helen Beggs, Ian Grooms, Patrice Klein, Andrew Majda, and Aurelien Ponte. SRK was supported by a UNSW Faculty Research Grant. SRK is also an Associate Investigator in the ARC Centre of Excellence in Climate Systems Science which is supported by the Australian Research Council via grant CE110001028. KSS was supported by NSF grant OCE-0962054. In compliance with the AGU Data Policy, the data and code used in this research will be made available on request from Dr. Shane Keating (s.keating@unsw.edu.au).

References

Blumen, W. (1978), Uniform potential vorticity flow: Part I. Theory of wave interactions and two-dimensional turbulence, *J. Atmos. Sci.*, *35*, 774–783.

Bowen M. M., W. J. Emery, J. L. Wilkin, P. C. Tildesley, I. J. Barton, and R. Knewston (2002), Extracting multiyear surface currents from sequential thermal imagery using the maximum cross-correlation technique, *J. Atmos. Oceanic Technol.*, *19*, 1665–1676.

Branicki, M., and A. J. Majda (2013), Dynamic stochastic superresolution of sparsely observed turbulent systems, *J. Comput. Phys.*, *241*, 333–363.

DelSole, T. (2004), Stochastic models of quasigeostrophic turbulence, *Surv. Geophys.*, *25*, 107–149.

Emery, W. J., A. C. Thomas, M. J. Collins, W. R. Crawford, and D. L. Mackas (1986), An objective method for computing advective surface velocities from sequential infrared satellite images, *J. Geophys. Res.*, *91*(C11), 12,865–12,878.

Ferrari, R., and C. Wunsch (2009), Ocean circulation kinetic energy: Reservoirs, sources, and sinks. *Annu. Rev. Fluid Mech.*, *41*, 253–282.

Forget, G. (2010), Mapping ocean observations in a dynamical framework: A 2004-05 ocean atlas, *J. Phys. Oceanogr.*, *40*, 1201–1221.

Harlim, J., and A. J. Majda (2008), Mathematical strategies for filtering complex systems: Regularly spaced sparse observations, *J. Comput. Phys.*, *227*, 5304–5341.

Harlim, J., and A. J. Majda (2010), Filtering turbulent sparsely observed geophysical flows, *Mon. Weather Rev.*, *138*(4), 1050–1083.

Held, I. M., R. T. Pierrehumbert, S. T. Garner, and K. L. Swanson (1995), Surface quasi-geostrophic dynamics, *J. Fluid Mech.*, *282*, 1–20.

Hoskins, B. J., I. Draghici, and H. C. Davies (1978), A new look at the omega-equation, *Q. J. R. Meteorol. Soc.*, *104*, 31–38.

Hoskins, B. J., M. E. McIntyre, and A. W. Robinson (1985), On the use and significance of isentropic potential vorticity maps, *Q. J. R. Meteorol. Soc.*, *111*, 877–946.

Holyer, R. J., and S. H. Peckinpaugh (1989), Edge detection applied to satellite imagery of the oceans, *IEEE Trans. Geosci. Remote Sens.*, *27*, 46–56.

Isern-Fontanet, J., B. Chapron, G. Lapeyre, and P. Klein (2006), Potential uses of microwave sea-surface temperatures for the estimation of ocean currents, *Geophys. Res. Lett.*, *33*, 24608, doi:10.1029/2006GL027801.

Isern-Fontanet, J., G. Lapeyre, P. Klein, B. Chapron, and M. W. Hecht (2008), Three-dimensional reconstruction of oceanic mesoscale currents from surface information, *J. Geophys. Res.*, *113*, C09005, doi:10.1029/2007JC004692.

Kalman, R. E. (1960), A new approach to linear filtering and prediction problems, *J. Basic Eng.*, *82*, 35–45.

Keating, S. R., A. J. Majda, and K. S. Smith (2012), New methods for estimating ocean eddy heat transport using satellite altimetry, *Mon. Weather Rev.*, *140*(5), 1703–1722.

Klein, P., J. Isern-Fontanet, G. Lapeyre, G. Roullet, E. Danioux, B. Chapron, S. Le Gentil, and H. Sasaki (2009), Diagnosis of vertical velocities in the upper ocean from high resolution sea surface height, *Geophys. Res. Lett.*, *36*, L12603, doi:10.1029/2009GL038359.

Kuznetsov, L., K. Ide, and C. K. R. T. Jones (2003), A method for assimilating Lagrangian data, *Mon. Weather Rev.*, *131*(10), 2247–2260.

LaCasce, J. H., and A. Mahadevan (2006), Estimating subsurface horizontal and vertical velocities from sea-surface temperature, *J. Mar. Res.*, *64*, 695–721.

Lapeyre, G. (2009), What vertical mode does the altimeter reflect? On the decomposition in baroclinic modes and on a surface-trapped mode, *J. Phys. Oceanogr.*, *39*, 2857–2874.

Lapeyre, G., and P. Klein (2006), Dynamics of the upper oceanic layers in terms of surface quasigeostrophy theory, *J. Phys. Oceanogr.*, *36*, 165–176.

Majda, A. J., and M. J. Grote (2007), Explicit off-line criteria for stable accurate time filtering of strongly unstable spatially extended systems, *Proc. Natl. Acad. Sci. U. S. A.*, *104*, 1124–1129.

Majda, A. J., and J. Harlim (2012), *Filtering Complex Turbulent Systems*, Cambridge Univ. Press, Cambridge, U. K.

Marshall, J., A. Adcroft, C. Hill, L. Perelman, and C. Heisey (1997), A finite-volume, incompressible Navier-Stokes model for studies of the ocean on parallel computers, *Geophys. Res. Lett.*, *102*(C3), 5753–5766.

Munk, W., P. Worcester, and C. Wunsch (1995), *Ocean Acoustic Tomography*, Cambridge Univ. Press, Cambridge, U. K.

Rauch, H. E., F. Tung, and C. T. Striebel (1965), Maximum likelihood estimates of linear dynamical systems, *AIAA J.*, *3*(4), 1445–1450.

Roullet, G., J. C. McWilliams, X. Capet, and M. J. Molemaker (2012), Properties of steady geostrophic turbulence with isopycnal outcropping, *J. Phys. Oceanogr.*, *42*, 18–38.

Shcherbina, A. Y., E. A. D'Asaro, C. M. Lee, J. M. Klymak, M. J. Molemaker, and J. C. McWilliams (2013), Statistics of vertical vorticity, divergence, and strain in a developed submesoscale turbulence field, *Geophys. Res. Lett.*, *40*, 4706–4711, doi:10.1002/grl.50919.

Sheen, K. L., et al. (2013), Rates and mechanisms of turbulent dissipation and mixing in the Southern Ocean: Results from the Diapycnal and Isopycnal Mixing Experiment in the Southern Ocean (DIMES), *J. Geophys. Res. Oceans*, *118*, 277–2792, doi:10.1002/jgrc.20217.

Smith, K. S., and J. Vanneste (2013), A surface-aware projection basis for quasigeostrophic flow, *J. Phys. Oceanogr.*, *43*, 548–562.

Thomas, L. N., A. Tandon, and A. Mahadevan (2008), Submesoscale processes and dynamics, in *Ocean Modeling in An Eddying Regime, Geophys. Monogr. Ser.*, vol. 177, edited by M. W. Hecht and H. Hasumi, AGU, Washington, D. C.

Tulloch, R., J. Marshall, C. Hill, and K. S. Smith (2011), Scales, growth rates and spectral fluxes of baroclinic instability in the ocean, *J. Phys. Oceanogr.*, *41*(6), 1057–1076.

Wang, J., G. R. Flierl, J. H. LaCasce, J. L. McClean, and A. Mahadevan (2013), Reconstructing the ocean's interior from surface data. *J. Phys. Oceanogr.*, *43*(8), 1611–1626.

Wunsch, C. (2006), *Discrete Inverse and State Estimation Problems*, Cambridge Univ. Press, Cambridge, U. K.